PPPL-3178 - Preprint Date: May 1996, UC-420, 426

The Effect of Toroidal Field Ripple on Confined Alphas in TFTR D-T Plasmas

H.H. Duong,[a] R.K. Fisher, S.S. Medley,[b] M.P. Petrov,[c] N.N. Gorelenkov,[d] R.V. Budny,[b] D.K. Mansfield,[b] J.M. McChesney, P.B. Parks, A.L. Roquemore,[b] R.B. White,[b] S.J. Zweben[b]
General Atomics, San Diego, California, USA,
[a] General Atomics ORAU Fellow at Princeton
[b] Princeton Plasma Physics Laboratory, Princeton University, Princeton, New Jersey, USA
[c] Ioffe Physical-Technical Institute, St. Peterburg, Russia
[d] TRINITI, Troitsk, Russia

ABSTRACT. The Pellet Charge Exchange (PCX) diagnostic on the Tokamak Fusion Test Reactor (TFTR) presently measures trapped alpha distribution functions with very small pitch angle ($v_{||}/v \sim 0.05$) at the midplane. The measured PCX alpha signal exhibits a depletion region near the outboard region. Results of the alpha energy spectra and radial profile suggest stochastic ripple diffusion is the cause of the depletion. Comparison of the ripple stochastization boundary with Goldston-White-Boozer theory also shows the correct functional dependence on alpha energy and q-profile.

1. INTRODUCTION

Understanding the behavior of alpha particles in a burning plasma is essential for the design of fusion devices [1]. A large fraction of the alphas must be confined long enough to deposit a significant fraction of their energy in the plasma for fusion ignition to take place. In addition, even if a small ($\leq 10\%$) fraction of the energetic alphas is lost to the first wall, toroidal field ripple can localize these losses and create the possibility of first wall damage.

Prior to the Tokamak Fusion Test Reactor (TFTR) tritium experiments, alpha confinement physics has only been experimentally studied using 'alpha-like' fast ions such as neutral beam injected ions, radio-frequency accelerated ions, and fusion products from deuterium-deuterium fusion reactions. Although the results from these alpha simulations provide excellent guidelines, the need for direct measurements of alpha particles is genuine owing to differences between the fast ion species. The alpha population in TFTR tritium experiments is sufficiently large to provide the first real opportunity to study alpha particle behavior in a fusion plasma. The primary diagnostic of energetic ($E_a > 0.5$ MeV) confined alphas on TFTR is Pellet Charge Exchange (PCX). Previous papers have reported that alphas in the quiescent core of TFTR are well confined and slowing down classically [2]. The present geometrical configuration of PCX allows the instrument to detect escaping alphas along a highly perpendicular sight line; these alphas are very sensitive to toroidal magnetic field (TF) ripple.

The study of ripple losses is important for the design of tokamak-based fusion reactors because ripple transport is a strong function of the ripple amplitude. The choice of the number

of toroidal field coils in a tokamak is a compromise between minimizing ripple and choosing a smaller number of coils which enhances access for plasma heating, remote handling and plasma diagnostics. Although both theory and computational simulation predict negligible TF ripple induced alpha particle losses in a fusion reactor where the ripple amplitude is less than 1-2%[3,4], these losses are localized and may cause serious first-wall heat load problems in a reactor even if the losses are kept to a few percent [5]. In addition, there is some evidence that sawteeth [6,7] and other magnetohydrodynamic (MHD) instabilities [8] may transport alphas into the ripple loss regions and potentially increase the losses well above this level.

The primary mechanisms of TF ripple induced fast ion transport are direct ripple trapping, ripple plateau diffusion, ripple banana diffusion, and stochastic ripple diffusion [9]. In direct ripple trapping, the toroidal field ripples create secondary magnetic wells that can trap superbanana particles and cause them to drift vertically until they hit the vessel wall. Collisionless stochastic ripple diffusion occurs when the field ripples induce a random radial step of the banana orbit, mainly near the bounce point where the parallel velocity of the particle is small. When the banana tip displacement is sufficiently large to make the toroidal angle change between successive bounce points larger than the toroidal period $F(2\pi,N)$ (N = the number of TF coils) the radial steps become decorrelated, randomizing the motion, and diffusive loss of particles takes place. Assuming conservation of energy and magnetic moment, the banana tip moves vertically in a random walk fashion until the particle hits the vessel wall. The onset of stochastic motion cannot be accurately predicted by present day theory; however, a simplified analytical approximation for the stochastization threshold can be expressed as:

$$F(2d_{TF}\rho q',\pi)\, B(F(\pi Nq,\varepsilon))\, S(F(3,2))\, B(F(\theta_b + S^{-1}\cot\theta_b, R(\sin\theta_b))) \geq 1, \qquad (1)$$

where δ_{TF} is the magnetic field ripple, ρ the particle gyroradius, ε the inverse aspect ratio, q the safety factor, q'=F(dq,dr), S=rF(q',q) the magnetic shear, and θ_b the poloidal angle of the bounce point. Equation 1 is the midpoint of the 'fuzzy' stochastic boundary that corresponds to α = r(2) (see Eq. 13). Note that in the limit of θ_b=F(π,2), Eq. 1 reduces to the familiar Goldston-White-Boozer (GWB) threshold [10]

$$\delta_{TF}\rho q'\, B(F(\pi Nq,\varepsilon))\, S(F(3,2)) \geq 1. \qquad (2)$$

Ripple plateau and ripple banana diffusion both describe the process whereby the banana particle also suffers a radial displacement (ΔR) at its bounce position caused by field ripple. The diffusion arises when ΔR becomes decorrelated as the particle crosses a phase of the ripple well. Ripple plateau diffusion occurs when ΔR is decorrelated by collisionality ($\nu_{collision}$

$\geq \nu_{bounce}$) [1]. Ripple banana diffusion exists between the collisionless regime and ripple plateau diffusion where $\nu_{collision} < \nu_{bounce}$ [1]. Of the four, the most dominant mechanism on TFTR is stochastic ripple loss.

Owing to the complexity of fast ion orbits, an accurate calculation of ripple losses requires time consuming computational simulations using complex computer codes. Presently, there exist several ripple models and calculation techniques [11-13] developed to calculate ripple losses in contemporary tokamaks. Once these models are compared with realistic experimental results, they can be used to aid the design of future reactors such as ITER.

Previous ripple experiments utilize indirect diagnostic techniques for assessing the effect of ripple on alpha confinement, either by monitoring the fusion produced neutron emission or by capturing the escaping charged fusion products. Boivin et al. performed the first studies of stochastic ripple diffusion on TFTR [14]. The probe used in the study employed scintillators to measure the pitch angle and energy of escaping D-D fusion products. The inferred stochastic ripple threshold was one to three times the value predicted by GWB. On JT-60U, Tobita et al. used the neutron emission and measurement of hot spots on the vessel wall to assess beam ion losses due to ripple [5]. The goal of the study was to assess the validity of the modeling of a guiding center orbit following Monte Carlo (OFMC) code developed by Tani et al. [15]. The observed parametric dependence of the decay in neutron emission showing enhanced losses for trapped beam injection suggests TF ripple influence. With the inclusion of the toroidal electric field, the OFMC predicted both ripple trapping and banana drift loss fairly well by reconstructing the temporal dependence of the neutron emission. Similar results were obtained with infra-red camera measurement of heating on the vessel wall. There the OFMC prediction reconstructed both the measured hot spot position and heat flux with reasonable accuracy.

Sadler et al. performed a controlled ripple experiment on JET where they increased the ripple at the outboard limiter from 1% up to 12.5% [16]. The energetic test particles were RF-accelerated ions and tritons from D-D fusion. Measurements of RF-accelerated ions using a high energy neutral particle analyzer showed no evidence of stochastic ripple diffusion. Triton burnup was anomalously lower than predicted by stochastic diffusion theory but uncertainties were high with poor data statistics. In TFTR, Zweben et al. recently observed losses of DT alphas near the midplane where collisionless stochastic ripple diffusion is dominant [17]. Complimentary to these lost alpha measurements, confined alpha measurements obtained by the PCX diagnostic show an alpha depletion region in phase space that is consistent with ripple theories [6]. The PCX measurements allow for a direct mapping of the ripple boundary on the midplane for alpha particles inside the plasma.

The ability of the PCX diagnostic to measure radially resolved alpha energy spectra provides a unique opportunity to study the effect of TF ripple on the confined alpha distribution *in* the plasma. This paper discusses the first detailed experimental study of the TF ripple

effects on alpha particles in a fusion plasma. The paper is divided into 5 sections. In Section 2 and 3 we briefly review the experimental technique and models used for analysis. In Section 4 we describe the data used for the study, and in Section 5 analyses of the results are presented. Finally, a summary is given in Section 6.

2. DESCRIPTION OF PCX DIAGNOSTIC

A Lithium Pellet Injector (LPI) and a Neutral Particle Analyzer (NPA) are the primary components of the PCX diagnostic on TFTR. A linear photodiode array situated on the top of the TFTR vacuum vessel measures the radial position and velocity of the injected pellet. Data from PCX combined with the photodiode array allow us to obtain radially resolved energy spectra and density profiles. The LPI injects cylindrical impurity pellets of dimension 2 mm (diameter) by 3 mm (length); each pellet contains approximately 10^{19}-10^{20} atoms. The injector uses helium, deuterium or hydrogen to propel the pellet to velocities of ≤650 m/s. When injected into the plasma, the pellet ablates forming a toroidally extended ablation cloud. The cloud provides a dense target in which alphas incident on the cloud are converted to helium neutrals via electron capture processes. The escaping helium neutrals are subsequently detected by an E || B NPA with eight discrete energy channels equipped with ZnS(Ag) scintillators. The light emission from the scintillators is measured by photomultiplier tubes. In the present configuration, the NPA sight line is fixed to view the radially injected pellets from behind at a toroidal angle of 2.75^{o} to the pellet trajectory. A neutron shield consisting of four inches of lead and six inches of borated polyethylene is used to reduce the neutron background noise. The shield attenuates D-D and D-T neutrons by a factor of ~500 and ~100 respectively. The energy dependence of the incident alphas dn_{He+}/dE can be determined from the measured energy distribution of the energetic helium neutrals dn_{He+}/dE using

$$dn_{He+}/dE = F(dn_{He0}/dE, F_0(E)) \qquad (3)$$

where $F_0(E)$ is the fraction of alphas neutralized in the cloud, as discussed in reference [1]. An improved calculation of the alpha-cloud interactions, which includes the helical nature of the incident alpha orbits, is described in reference 18.

3. ALPHA DISTRIBUTION MODELS

Modeling of alpha distributions for realistic plasmas requires time consuming calculations using complex codes. The primary plasma analysis code used for TFTR is TRANSP [19,20]. TRANSP is a 1F(1,2)-dimensional transport code (calculations of magnetic equilibrium are two-dimensional) that uses measured plasma parameters with minimal additional

assumptions to model plasma discharges. In TRANSP, the electron temperature is obtained from electron cyclotron emission [21], electron density from infrared interferometry [22], and ion temperature and toroidal rotational velocity from charge exchange spectroscopy [23]. The recycling of wall neutrals and Z_{eff} (assumed radially flat) are inferred from spectroscopic measurement of the D_α emission and visible Bremsstrahlung data [24]. Monte Carlo techniques are used to calculate neutral beam parameters [19]. A time dependent Monte Carlo TRANSP Processor (MCTP) code which follows the alpha orbits as they thermalize is then used to deduce the full alpha energy and radial distribution. TRANSP provides a good calculation of the alpha distribution integrated over all pitch angles. The code assumes alphas slow down classically and was recently modified to include ripple effects [13]. The TRANSP ripple model uses the GWB formalism with an adjustable coefficient. The TRANSP ripple model approximately calculates the effect of ripple on global alpha parameters, not detailed phase space profiles.

In light of the limitations of TRANSP, we developed the Fokker-Planck Post TRANSP (FPPT) processor code. The code is based on the Fokker-Planck formalism and uses the radial and energy profiles of the pitch angle integrated alpha source from TRANSP to calculate alpha distributions for experimental conditions specific to the PCX measurements. The FPPT code assumes that for the processes with characteristic times greater than the α–particle bounce period, which is $\tau_b \sim 10^{-6}$ s in TFTR, the distribution function of α-particles can be represented as a function of particle constants of motion versus time:

$$f_\alpha = f_\alpha (v, \mu, P_\varphi) \qquad (4)$$

where

$$\mu = F(m(1 - v_{||}/v)^2,2B), \quad P_\varphi = F(e_\alpha\psi,2\pi m_\alpha c) – F(v_{||}RB_\varphi,B); \qquad (5,6)$$

where ψ is the poloidal magnetic flux. The corresponding drift orbit averaged Fokker- Planck equation for the α- particle distribution function is [25]

$$F(\partial f_\alpha,\partial t) = <S\ t\ (f_\alpha)> + <S_\alpha> - F(f_\alpha,\tau_\delta)\ , \qquad (7)$$

where <...> denotes the time averaging over the α-particle drift orbit, and

$$S_\alpha = S_{TR}(r,t)\ F(\exp(– (v\text{-}v_{\alpha 0})^2/vS(_{2,T})),r(\pi)vs(_{2},\alpha 0)v_T) \qquad (8)$$

is the α-particle source with $S_{TR}(r,t)$ taken from the TRANSP code, and v_T is the Doppler

broadening. Equation 8 assumes Maxwellian distributions for the interacting species and gives a good approximation for beam-target interactions [26]. The collisional integral given by

$$St(f_\alpha) = F(1,v^2\tau_s)\, F(\partial(v^3 + vs_{(3,*)})f_\alpha,\partial v) + F(1,\tau_s)\left(P_\varphi - F(e_\alpha\psi,2\pi m_\alpha c)\right)\left(1 + F(vs_{(3,*)},v^3)\right) F(\partial f_\alpha,\partial P_\varphi), \quad (9)$$

where τ_s is the slowing down time, describes only the slowing down of alphas and does not include scattering and velocity diffusion [25]. The last term in Eq. 7 is introduced to account for the stochastic ripple losses, with τ_δ being the approximate confinement time associated with this loss process. The term τ_δ was derived by Yushmanov [4] and takes the form

$$\tau_\delta = F((a - r)^2,D_\perp) \quad (10)$$

where

$$D_\perp = F((\Delta r)^2,\tau_b) \text{ is the diffusion coefficient,} \quad (11)$$

$$(\Delta r)^2 = F(\pi\rho^2q^3N\delta^2(r_b,\theta_b),2\varepsilon^3 \sin\theta_b\,[1+ \exp(6.9 - 5.5\alpha)]) \quad (12)$$

and

$$\alpha = B(F(8\pi N^3q^5R^3,\omega s_{(2,c)}r^5))s(^{1/2},)\; v\; \delta(r_b,\theta_b)F(\theta_b\, S + \cot\theta_b,\, R(\sin\theta_b)). \quad (13)$$

In Eq. 11, Δr is the radial step size during one bounce period and r_b, θ_b are the radial and poloidal coordinates of the banana tip, respectively. Note when $\alpha = r(2)$, which implies that we are in the stochastic “transition” region, we recover Eq. 1.

In the TFTR, δ_{TF} is well represented by the expression:

$$\delta_{TF}(r,\theta) = \delta_0\, expB(F([(R_0 + r\cos\theta - R_{rip})^2 + b_{rip}(r\sin\theta)^2]^{1/2},w_{rip})), \quad (14)$$

where R_0 is the major radius, $R_{rip} = 2.25$ m, $b_{rip} = 1.31$, $w_{rip} = 0.1657$ m, $\delta_0 = 6.0 \times 10^{-5}$, and $N = 20$. In the case of deeply trapped alpha particles [27],

$$\sin^2(\theta_b/2) = F(\lambda^2(1 + \varepsilon) + \zeta\lambda,2(\varepsilon + \zeta\lambda)) \quad (15)$$

where $\lambda = F(v_{||},v)$ is the velocity pitch and $\zeta = F(\rho_\theta,R_0)$ is the ratio of the poloidal gyroradius to the major radius of the magnetic axis. The FPPT code solves Eq. 4 numerically by the method of integration over the particle characteristics [28]. Direct guiding center orbit averaging was

performed using TRANSP equilibrium along the drift orbit of α- particle determined by three constants of motion v, μ, and P_φ. With the ripple model turned off in both codes, the FPPT alpha distributions agree with TRANSP Monte Carlo calculations.

4. DESCRIPTION OF MEASUREMENTS

The plasmas used for the present study were deuterium-tritium (D-T) TFTR supershot discharges with 5.0 Tesla toroidal field. Plasma major radii of 2.45 m and 2.52 m were used. The plasma current varied from Ip = 1.3 - 2.0 MA; there were two discharges where the current was ramped up from 0.6 to 1.4 MA and ramped down from 2.2 to 1.4 MA. The peak electron densities were about 5.0 x 10^{19} m^{-3} for the constant current discharges, and 2.0 x 10^{19} m^{-3} when the current was ramped. The peak electron temperatures ranged from 8 to 16 keV for the constant current cases and was approximately 5 keV for the current ramps. The plasmas were heated by a mixture of deuterium and tritium neutral beam injection (NBI) ranging from 7 MW to 20 MW. The peak DT neutron emission was about 1.2 x 10^{18} s^{-1} for constant currents and 1.4 x 10^{17} s^{-1} for ramped currents.

The time evolution of the main plasma parameters for a 2.0 MA discharge is shown in Fig. 1. The integrated central alpha density is calculated by TRANSP. The deuterium target plasma was heated by a mixture of deuterium and tritium beams with P_{inj} = 20 MW. The peak neutron emission was 1.20 x 10^{18} s^{-1}. A pair of lithium pellets was fired at ~300 ms after the turn off of neutral beams in a stacked fashion separated by τ_{sep} ~ 10 ms. At the time of pellet injection the core electron temperature was ~ 7.25 keV and the electron density was 2.80 x 10^{19} m-3. Firing the pellets after NBI allows for better pellet penetration owing to lower electron temperature with a more narrow profile (Fig. 2). Stacking the pellets further enhance penetration of the second pellet [29] and τ_{sep} is short enough not to disturb the alpha distribution ($\tau_{sep} << \tau_{sl}$; τ_{sl} ~ 230 ms at pellet injection time). While the first pellet penetrated poorly (R_p ~ 2.85 m), it lowered the plasma electron temperature sufficiently to allow the second pellet to penetrate to R_p ~ 2.42 m.

Figure 1 also includes the raw signals from the light emission of the pellet and the neutral alphas detected by the PCX analyzer. The light emission signal shows the visible light emitted by that portion of the pellet ablation cloud in the field of view of the NPA. The neutral signal represents helium neutral flux from alpha-cloud interactions. The pellets are injected perpendicularly into the plasma at the midplane and have lifetime of less than 2 ms. The start of the light signal approximately corresponds to the time that the pellet reaches the outer edge of the plasma. A common feature of all the PCX data is the existence of a delay in the rise of the alpha signal relative to the light signal. In other words, we do not observe an alpha signal until the pellet penetrates beyond a certain plasma radius. The depleted region of alpha signal is observed in all discharges with PCX data. As we will show in the following

section, this depleted alpha signal region is due to stochastic ripple diffusion.

5. DATA ANALYSIS AND DISCUSSION

The existence of the depleted alpha signal region is best explained by examining the alpha loss region in phase space. Figure 3 is a mapping of the 3.5 MeV alpha loss boundary in pitch angle and major radius space for a 1.4 MA TFTR supershot discharge. The figure is the result of an orbit following calculation using the Hamiltonian formalism developed by White et al. [11]. The code imposes a vacuum field ripple δ onto an axisymmetric poloidal field given by a MHD equilibrium. The field ripple δ takes the same form as that used in the FPPT code (see Sec. 2). The pitch angle and major radius scan is produced by following the 3.5 MeV alpha particle guiding center in the "TF-rippled" equilibrium for an alpha slowing down time. Simulations were performed without ripple (first orbit loss only), with ripple, and with ripple and collisionality. From the figure, we can see that TF ripple opens up a loss region for perpendicular orbits. The addition of collisonality essentially widens the loss region, particularly with midplane $F(v_{||},v) \sim 0$. The PCX diagnostic, in its current geometrical configuration, provides a radial scan at $F(v_{||},v) \sim 0.048$ on this map. This simulation produces a snap shot of the alpha loss boundary and can only be use for qualitative comparisons with the PCX data. However, the comparison provides an excellent guide in understanding the physical cause for the depletion of PCX alpha signal near $F(v_{||},v) \sim 0$.

5a. Ripple influence on energy spectra and radial profiles

For detail analysis of the PCX data, we adopt the time dependent code FPPT. Figure 4 illustrates the alpha energy spectra at two different major radii, R = 2.58 m (near the plasma center) and R = 2.70 m. Since the PCX diagnostic does not provide an absolute measurement of the alpha density, the experimental data are normalized to the theoretical model at E_α = 1.0 MeV. The FPPT calculations shown here are for a specific midplane pitch angle, in this case $F(v_{||},v) = 0.048$. Also shown in the figure are the FPPT predictions of the alpha energy spectrum without ripple effects. The first observation from the comparison is that the ripple influence is stronger at R=2.70 m than near the plasma center. This is not surprising since the ripple amplitude dTF is largest near the outer midplane. Near the plasma center where δ_{TF} is small, the difference between the two FPPT comparisons is negligible and shows the accuracy of the FPPT ripple model (Eq. 7). Near the outer midplane, the shape and amplitude of the PCX energy spectrum is in better agreement with the version of FPPT that includes ripple.

Another less intuitive result is the flattening of the measured energy profile at R = 2.70 m. Experimentally we measured fewer alphas at lower energies (Ea £ 1.5 MeV) than expected from classical behavior, i.e., TF ripple depletes the low energy population. The func-

tional dependence of the ripple threshold (see Eq. 1) indicates that particles with larger gyroradius (higher energy) should be more affected by ripple. However, in this particular case, we see a stronger ripple influence at lower energies. Several mechanisms can flatten the energy profile.

One possible mechanism is the broadening of the alpha birth energy distribution due to the kinetic energy of the reacting ions [30]. Alphas are not born with a delta function at 3.52 MeV but with a distribution in energy space so that some of the alphas we observe in the higher energy portion of Fig. 4 may be birth alphas. In the FPPT code, we assume that the total alpha birth energy distribution is Doppler broadened by a Maxwellian plasma with an effective temperature T. The value for T is determined from the measured D-T neutron broadening [26]. The actual alpha birth energy distribution in TFTR is modified because a significant portion of the alphas is created by beam-target reactions; however, the difference is generally within 10% for TFTR plasmas [26]. With the inclusion of the broadened alpha distribution, it is conceivable that some of the higher energy alphas measured by PCX are not thermalized alphas but birth alphas. Accordingly, these birth alphas near 2.0 MeV are more likely to charge exchange with the pellet cloud before they are lost by stochastic ripple diffusion. However, this mechanism is unlikely to be the cause for the flattening of the energy spectrum because the generation of alphas is low at the pellet injection time. The neutron emission indicates that the alpha production rate is ~ 20 times lower at the pellet time than at the termination of NBI. Furthermore, the effect of the broadening of the alpha birth energy distribution is included in the FPPT calculation. Figure 4 clearly shows that the shape of the PCX spectrum deviates from FPPT without ripple at low energy. Hence, the effect of broadening of birth alphas cannot explain the flatness of the energy spectrum.

Another possible explanation is the population of alphas that generate low energy alphas with $F(v_{||},v) = 0.048$ near the plasma edge are lost before they fully thermalize owing to direct ripple trapping. Alphas with $E_\alpha = 0.5$ MeV and $F(v_{||},v) = 0.048$ at pellet firing time are generated by a class of alphas with very small θ_{bounce}. This class of particles is sensitive to direct ripple trapping, particularly at larger major radii where the ripple trapping loss cone is large. Particles affected by ripple trapping are lost within a few hundred transits; therefore this class of particles cannot build up a classical population in their appropriate phase space. This effect probably also plays a minor role in flattening the energy spectrum at R = 2.70 m.

The most likely explanation for the observed flattening of the energy spectrum at larger plasma radii is found by examining the relationship between the alpha confinement time τ_c ($\tau_c = \tau_\delta$ in the presence of toroidal ripple, see Eq. 7) and the alpha slowing down time τ_s. When the confinement time of the alphas is small compared to their slowing down time, energetic alphas are lost before they can thermalize, and do not build up a population of lower energy alphas (see Fig. 5a). When τ_c is comparable to τ_s, high energy alphas are sufficiently confined to build up a small alpha population at low energy. This effectively produces a flat

energy spectrum as shown in Fig. 5b. In the case where the alpha confinement time is larger than their slowing down time, the alphas are able to fully thermalize and build a large alpha population at lower energy to produce an energy spectrum with an approximate Ea^{-1} dependence. Figure 5c portrays such phenomenon. At larger plasma radii, the alpha confinement time is reduced due to larger toroidal ripple; hence, for the case shown in Fig. 4, $F(t_c, \tau_s)$(R=2.70 m) < $F(\tau_c, \tau_s)$(R=2.58 m). The poorer alpha confinement time at R=2.70 m effectively produces a flatter energy spectrum as compared to that at R=2.58 m.

A complementary mechanism is the transient characteristic of the discharge. The pellets are fired at 300 ms after NBI when the plasma parameters exhibit dramatic time dependent changes. The plasma axis is moving inward due to the decrease in the Shafranov shift as the plasma pressure falls. At the firing of the pellets, the magnetic axis is at R = 2.62 m; however, at earlier times, the magnetic axis is further out in a region where the ripple amplitude is stronger. Because it takes longer for alphas to slow down from birth energy to 0.5 MeV than 2.0 MeV, particles that generate the 0.5 MeV alphas at the pellet time are born at a much earlier time when the plasma is displaced further out in a stronger ripple region. Particles that generate the 2.0 MeV alphas are born at a later time in a weaker ripple region because the Shafranov shift is smaller; hence they are confined longer. This effect also flattens the energy spectrum at larger plasma radii. Both mechanisms, particle confinement time and Shafranov shift, are accurately modeled by the time dependent FPPT code.

The radial profile of the 1.0 MeV alphas from the same discharge shown in Fig. 4 is plotted in Fig. 6. The data are smoothed over 50 μs to improve statistics. Special care must be taken in analyzing the alpha density profile owing to the possible variation of the fraction of alphas neutralized in the ablation cloud with major radius. The neutralization fraction is sensitive to the mixture of cloud ionization state. This mixture may change with the radial variation of the tokamak plasma electron temperature and density. It is important to note that these uncertainties should not affect measurements of the energy spectra [2,17]. Significant changes in the mixture of the charge state and in the pellet cloud size are expected near the end of the pellet's lifetime. These pellet burnout effects are the likely explanation for the lower than expected observed signal inside R=2.6 m in Fig. 4. The fluctuations in the PCX signal are not due to counting statistics and are observed in most discharges. These fluctuations are believed to be related to the fluctuations observed in the light emission from impurity and hydrogenic pellet clouds in a number of fusion experiments. Several theories have been proposed to explain the fluctuations. If a cloud instability, such as a Rayleigh-Taylor instability, causes the cloud to be displaced to a different set of magnetic field lines, the cloud will be quickly ionized to high ionization states [31]. This can result in a drop in the alpha neutralization fraction and hence in a drop in the PCX neutral signal. The fluctuation essentially reduces the neutral signal until new pellet ablation restores the cloud and the signal recovers. This

process can occur several times during the pellet life time.

Figure 4 compares the measured 1.0 MeV alpha signal with results from the FPPT code. Again both models, with and without ripple, are used in the comparison. The experimental data are normalized to the model at the peak PCX signal. Given the uncertainties discussed in the previous paragraph, the measured radial profile of the alpha population agrees with the FPPT calculation that includes ripple.

5b. Functional dependence of stochastic ripple threshold

It is interesting to examine the functional dependence of the stochastic ripple threshold as expressed in Eq. 1. Several key plasma parameters can change the ripple threshold. Two parameters of interest are the safety factor q and its radial derivative q´. Experimentally q and q´ can be modified by varying the plasma current on TFTR. The change in the radial location of the ripple boundary for different plasma current conditions is shown in Fig. 7. The figure shows the comparison between the PCX measured ripple boundary and the boundary determined by Eq. 1. The ripple boundary is defined as the major radius where the ripple threshold criteria of Eq. 1 are satisfied. Experimentally, this boundary is defined as the radial position where the alpha signals begin to appear on the PCX waveforms. The data set of Fig. 7 includes discharges with plasma current ranging from 1.3 MA to 2.0 MA. Within these plasma currents, the measured ripple boundary varied by about 10 cm. The corresponding TF ripple amplitude increased by about 40% from 1.8×10^{-4} to 3.0×10^{-4}. The comparison indicates that the measured boundaries are varying with q and q´ consistent with the scaling predicted by Goldston et al. However the measured boundaries consistently occur at smaller major radii than the theoretical prediction. On the average, the difference is ~ 6 cm. Such difference is not too surprising since the GWB criterion only provides an estimate of the stochastization threshold at which the particles are rapidly expelled. In practice, the ripple boundary need not be a sharp transition but a *soft* boundary described by finite diffusive process. Furthermore, the diffusion should occur near and below the stochastic threshold as suggested by Yushmanov et al. [4]. Another factor that may account for the difference is finite orbit effects. Eriksson et al. found significant modification of the GWB stochastization threshold for pinch orbits and trapped orbits with turning points near the horizontal midplane [12]. The former class of orbits does not apply to our PCX measurements since it describes large orbits with turning points in the high magnetic field side of the plasma. In their study, Eriksson et al. found that the deviation from GWB may be as large as an order magnitude in the threshold amplitude for these orbits. The data set of Fig. 7 also include a current ramp up and a current ramp down discharge. Ramping the current modifies the q profiles thereby shifting the ripple boundary. In this particular example, the measured effect of current ramp is negligible.

Next we examine the dependence of the ripple boundary on the alpha particle energy.

In quiescent discharges, where there is no radial redistribution of the alphas due to sawteeth activity, the ripple boundary is determined by the birth alpha energy. Experimentally, we observe the signals from all the PCX alpha energy channels appearing at approximately the same radial location (equivalently at ~ 6.28 x 10^{-4} sec in figure 8). Even though lower energy alphas have ripple loss boundaries at larger radii, there is no source of these lower energy alphas outside the 3.52 MeV boundary because the alphas born outside the 3.52 MeV boundary are lost before they can slow down. Hence the boundary for all energy alphas is determined by the ripple boundary at birth energy. Only when there is radial transport of alphas can lower energy alphas appear outside the birth energy boundary. These particles will then be confined based on the ripple boundary appropriate to their energy.

Large sawteeth that occur during the post neutral beam heating phase of TFTR discharges are observed to redistribute alphas all the way out to or past the stochastic ripple boundary of the lower energy alphas [6]. Hence, when we measure the alpha distribution after sawtooth instabilities, we observe alpha particles outside the birth energy ripple boundary. Furthermore, the onsets of the PCX measured alpha signals in different energy channels now appear at different radial locations which should reflect the stochastic ripple boundaries corresponding to their respective energies. Figure 9 shows the PCX measured ripple boundary for different alpha energies after sawtooth instabilities for two similar discharges. In the figure, the alpha distributions were measured after post beam sawtooth crashes. The alpha energy goes from 0.53 MeV to 1.21 MeV. In this range (Ea = 0.53 - 1.21 MeV), the neutral equilibrium fraction decreases from 4.99 x 10^{-2} to 1.20 x 10^{-2}; however, the analyzer detection efficiency increases from 0.05 to 0.18. Therefore, the effective instrumental response is relatively flat over the energy range of interest. We compare the PCX data to the GWB ripple model and note that experimental data have the same functional dependence on energy. Again the measured boundaries occur at smaller major radii than the predicted boundary. The difference between measurement and theory can be explained by the same arguments expressed earlier in the section. In addition, The GWB theory does not include the effect of slowing down. This may be an important factor since the data are taken approximately 120 ms after the sawtooth crash; this time is comparable to the alpha slowing down time. Finally, the data are taken after post beam sawteeth where the q profile is not known with good accuracy. Therefore, the predicted ripple boundary may be somewhat too large.

6. CONCLUSIONS

In summary, the first detailed measurements of the effects of toroidal field ripple induced stochastic diffusion on the *in situ* confined alpha particles in a tokamak are presented. Toroidal ripple induced loss, caused by stochastic diffusion, can account for the radial dependence of the alpha signals measured by the Pellet Charge Exchange diagnostic on TFTR.

Comparison between experimentally measured alpha energy distributions and the FPPT Fokker-Planck code, which was specially developed to calculate alpha distributions for PCX, shows good agreement when ripple effects are included in the calculations. Furthermore, the functional dependences of the stochastization threshold based on the GWB ripple formalism are supported by PCX measurements as a function of alpha energy and tokamak q-profile. The measured stochastic ripple threshold tends to be lower than the GWB threshold. The difference is probably due to finite orbit effects which are not included in the GWB theory.

ACKNOWLEDGMENTS

The authors gratefully acknowledge the contributions of the entire TFTR organization, the work by J.L. Terry. E. Marmar, and J. Snipes of the Massachusetts Institute of Technology in developing the lithium pellet injector and J. Felt for her help with the orbit code. One of us (H.H.D.) would like to express his appreciation for the contribution from Em Hanh.

This work was supported by the U.S. Department of Energy under Grant Nos. DE-FG03-92ER54150 and DE-FG02-84-ER53153, and by an appointment to the Research Participation Program at General Atomics administered by the Oak Ridge Associated Universities; such financial support does not constitute an endorsement by DoE of the views expressed herein.

REFERENCES

[1] HEIDBRINK, W.W., SADLER, G., Nucl. Fusion **34** (1994) 535.
[2] FISHER. R.K., et al., Phys. Rev. Lett. **75** (1995) 846.
[3] TANI, K., et al., Nucl. Fusion 23 (1983) 657.
[4] YUSHMANOV, P.N., Nucl. Fusion **23** (1983) 1599.
[5] TOBITA, K., et al., Phys. Rev. Lett. **69** (1992) 3060; TOBITA, K., et al., Nucl. Fusion **34** (1994) 1097.
[6] PETROV, M.P., et al., Nucl. Fusion **35** (1995) 1437.
[7] STRATTON, B.C., et al., "Effect of Sawteeth on Radial Profiles of Intermediate Energy Alpha Particles in TFTR Deuterium-Tritium Discharges," submitted to Plasma Physics and Controlled Fusion (1996).
[8] WHITE, R.B., et al., Phys. Plasma **2** (1995) 2871.
[9] YUSHMANOV, P.N., Review of Plasma Physics, Vol. 16, Consultants Bureau, New York (1966) 93.
[10] GOLDSTON, R.J., et al., Phys. Rev. Lett. **47** (1981) 647.

[11] WHITE, R.B., BOOZER, A.H., Phys. Plasma **2** (1995) 2915.
[12] ERIKSSON, L.-G., HELANDER, P., Nucl. Fusion **33** (1993) 767.
[13] REDI, M.H., et al., Nucl. Fusion **35** (1995) 1509.
[14] BOIVIN, R.L., et al., Nucl. Fusion 33 (1993) 449; BOIVIN, R.L. et al., Phys. Fluids B **5** (1993) 1559.
[15] TANI, K., et al., J. Phys. Soc. Japan **50** (1981) 1726.
[16] SADLER, G., et al., Plasma Physics and Controlled Fusion **34**, (1992) 1971.
[17] ZWEBEN, S.J., et al., Nucl. Fusion **35** (1995) 1445.
[18] McCHESNEY, J.M., PARKS, P.B., FISHER R.K., OLSON, R.E., "The Interaction of Fast Alpha Particles with Pellet Ablation Clouds," General Atomics Report, GA-A21958 (December, 1995).
[19] GOLDSTON, R.J., et al., J. Comput. Phys. **43** (1981) 61.
[20] BUDNY, R.V., Nucl. Fusion **32** (1992) 429.
[21] STAUFFER, F.J., et al., Rev. Sci. Instrum. **56** (1985) 925; TAYLOR, G., et al., Rev. Sci. Instrum. **56** (1985) 929; CAVALLO, A., et al., Rev. Sci. Instrum. **59** (1988) 889.
[22] MANSFIELD, D.K., et al., Appl. Opt. **26** (1987) 4469.
[23] BUSH, C.E., et al., Rev. Sci. Instrum **66** (1995) 1193; FONCK, R.J. et al., Phys. Rev. A **29** (1984) 3288.
[24] RAMSEY, A.T., TURNER, S.L., Rev. Sci. Instrum. **58** (1987) 1211.
[25] PUTVINSKII, S.V., Review of Plasma Physics, Vol. 18, Consultants Bureau, New York (1993) 239.
[26] KRASILNIKOV, A.V., et al., "Simulations and Analysis of Measured Energy Spectra of DT neutron emission in TFTR," Bulletin of the American Physical Society, **40** 11 (1995) 1768.
[27] PARKS, P.B., et al., Nucl. Fusion **35** (1995) 1297.
[28] GORELENKOV, N.N., PUTVINSKII, S.V., Sov. J. Plasma Phys. **15** (1989) 80.
[29] MEDLEY, S.S., et al., to be submitted to Rev. Sci. Instrument (1996).
[30] SADLER, G., et al., EPS (1995).
[31] PARKS, P.B., "Theory of Pellet Cloud Oscillation Striations," Rep. No. GA-A22005, General Atomics, CA (1995), accepted for publication in Plasma Physics and Controlled Fusion.

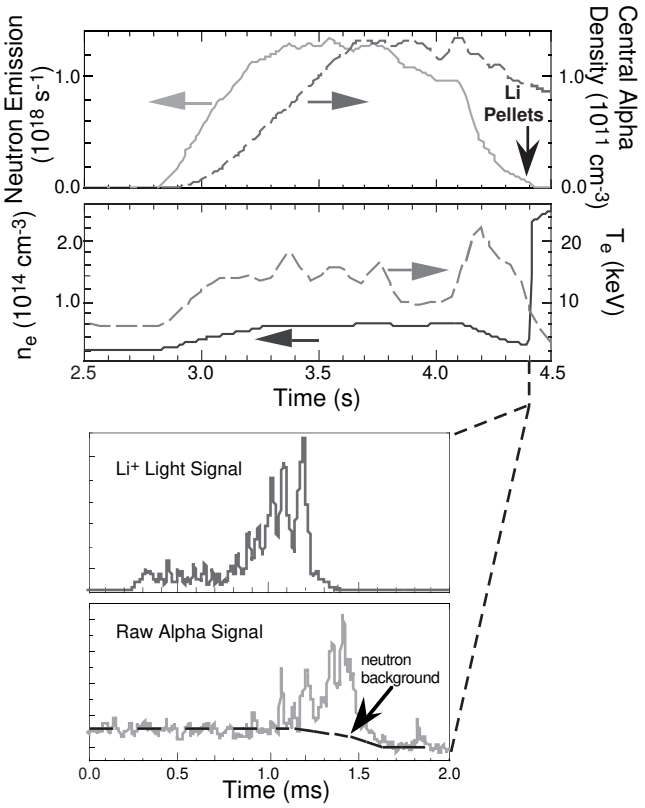

Fig. 1 Time evolution of the neutron emission, calculated alpha density, electron density and temperature, pellet light signal, and a sample of the raw alpha signal measured by PCX.

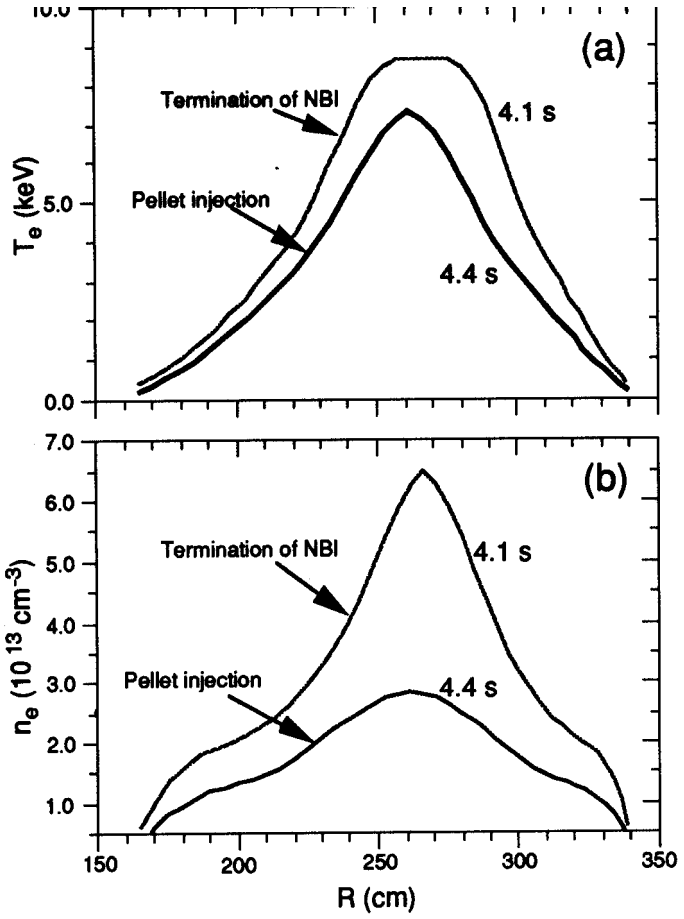

Fig. 2 The radial profiles of the electron temperature and density at the end of neutral beam injection (t = 4.1 s) and just before pellet injection time (t = 4.4 s). At the pellet injection time the electron temperature profile is lower at all plasma radii allows for better pellet penetration.

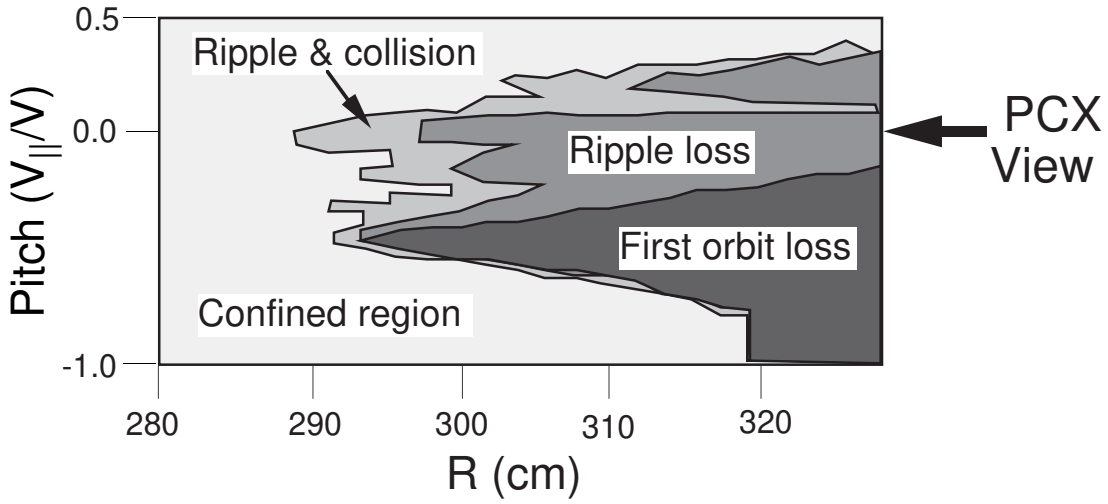

Fig. 3. Map the alpha loss boundaries in pitch angle and major radius space for the 3.52 MeV alpha particle. The map is created using a Hamiltonian orbit code that follows the alpha guiding center in the *rippled* plasma equilibrium for an equivalent slowing down time.

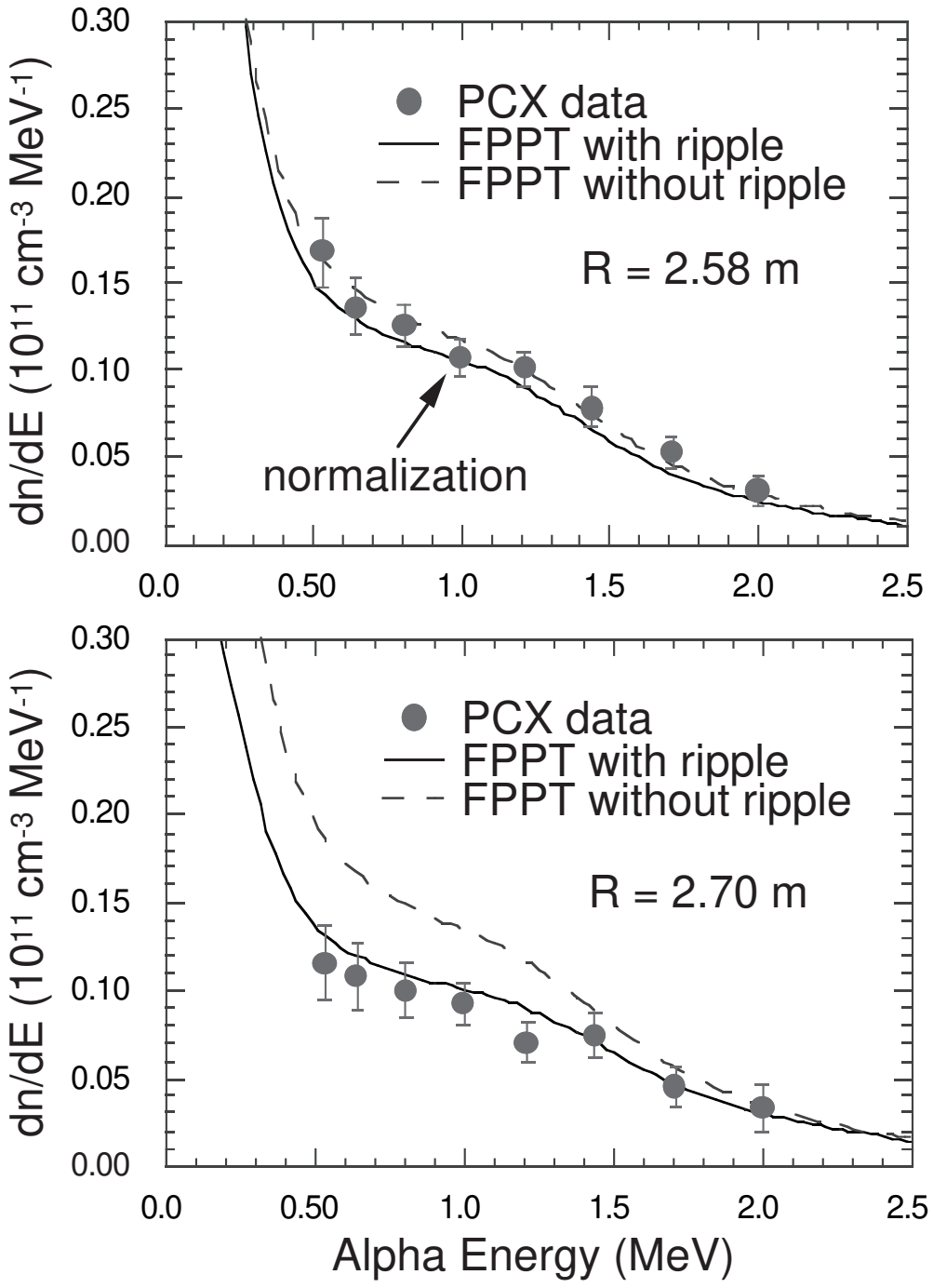

Fig. 4. Alpha energy spectra near the plasma center (R = 2.58 m) and the outboard midplane (R = 2.70 m) for the discharge described in Fig. 1. The PCX data are normalized to the FPPT code at 1.0 MeV. Ripple influence is stronger near the outboard midplane.

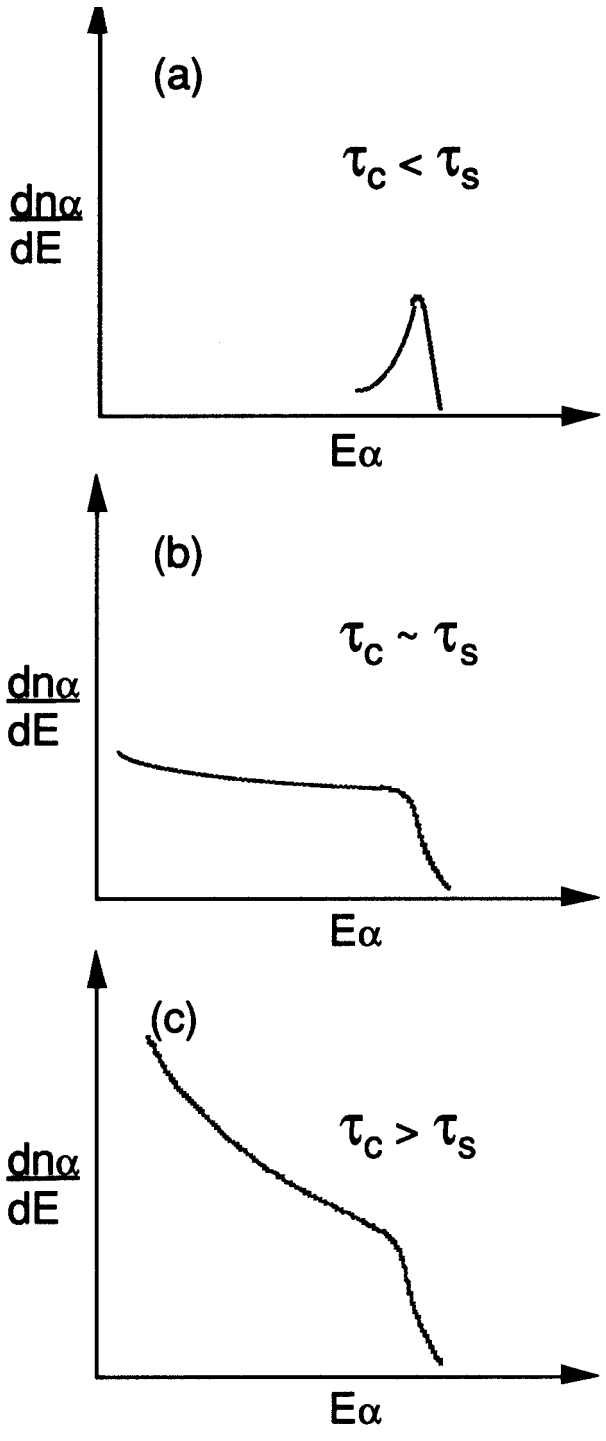

Fig. 5 Profiles depicting the possible alpha energy distribution for $\tau_c < \tau_s$ (a), $\tau_c \sim \tau_s$ (b), and $\tau_c > \tau_s$ (c).

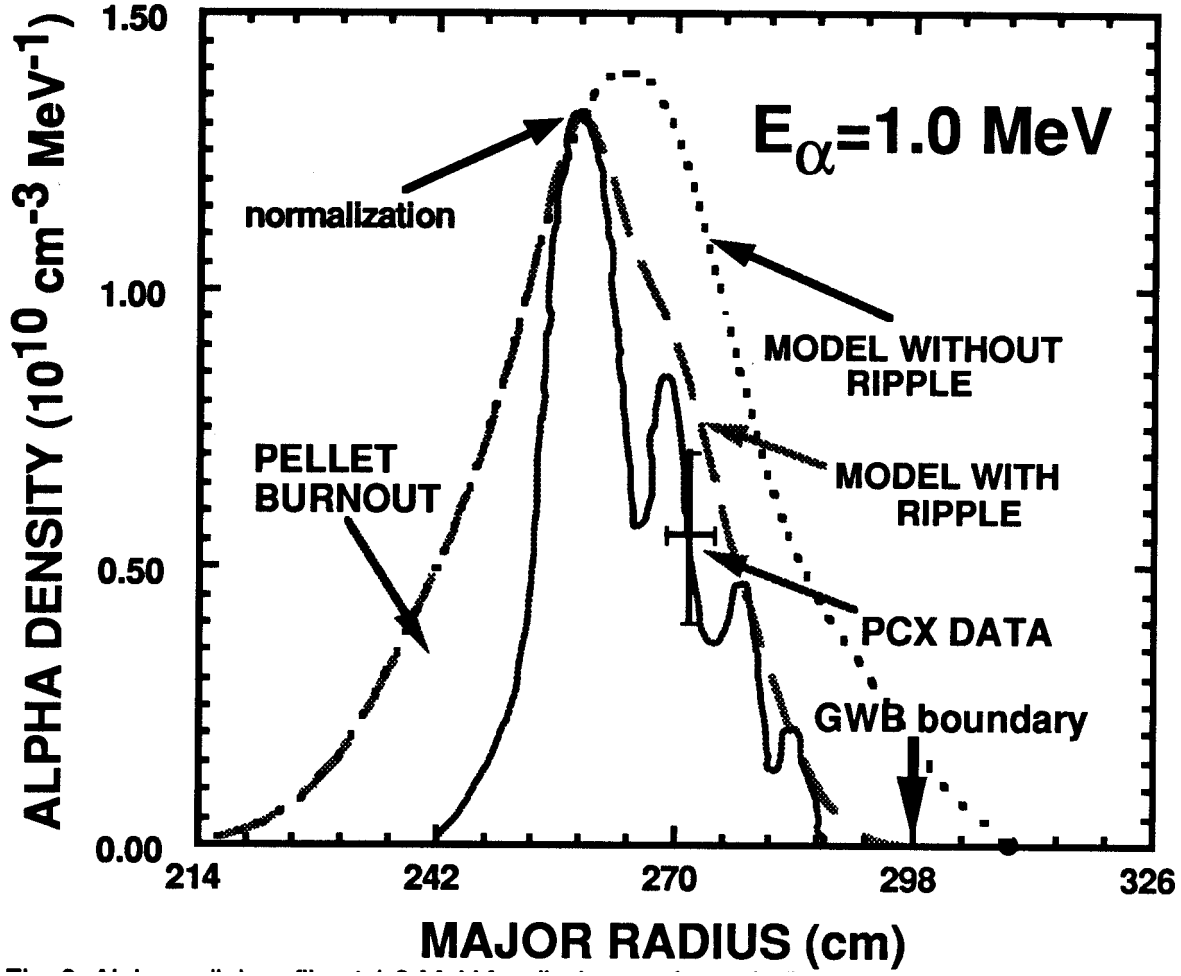

Fig. 6. Alpha radial profile at 1.0 MeV for discharge shown in figures 1 and 4. The PCX data is normalized to the FPPT code at peak of the profile. The measured profile agrees better with the ripple model. Also shown is location of the stochatization boundary based on the GWB formalism.

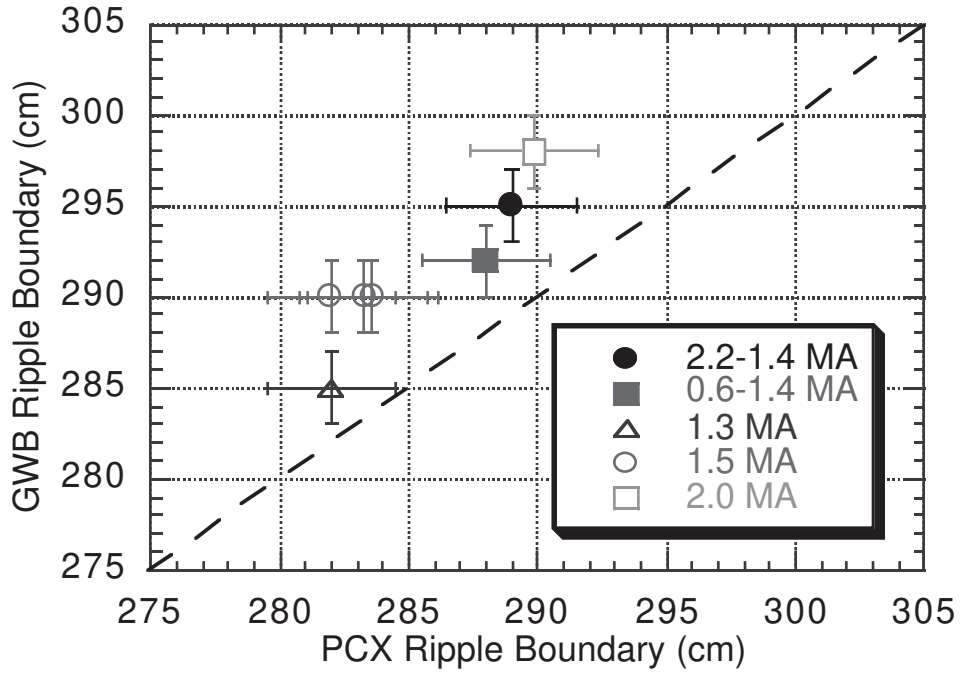

Fig. 7. Comparison of the stochastic ripple boundary between PCX and the GWB formalism at different plasma currents. Data represented by the solid circle and square are for discharge with current ramped down and up, respectively. The plasma major radius is R = 2.52 m except for the 1.5 MA discharges where R = 2.45 m.

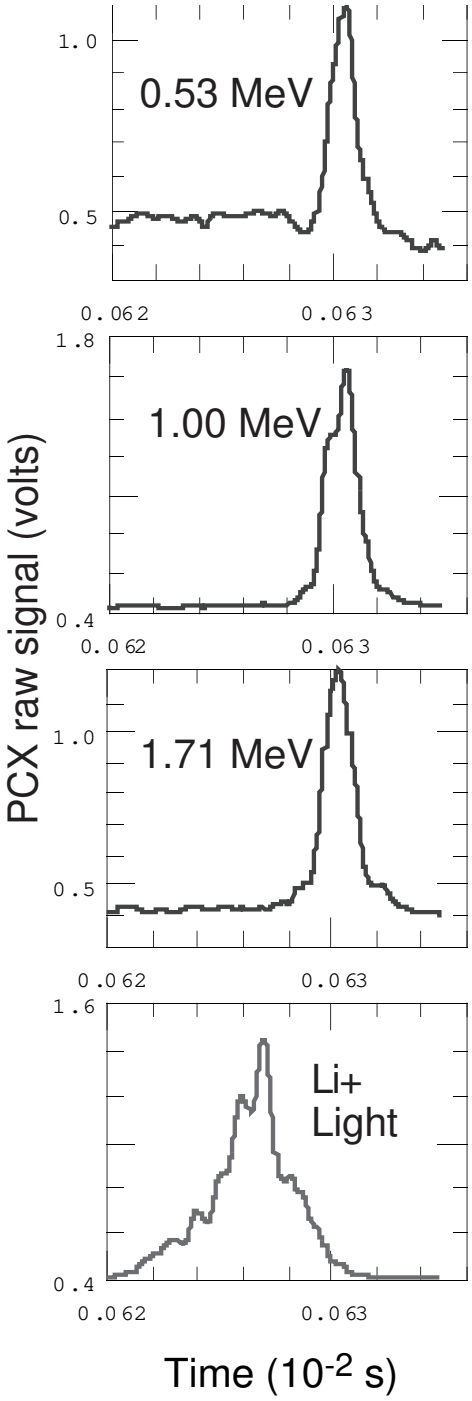

Fig. 8 Raw PCX waveforms for a sawtooth free discharge showing the same depletion region for all energy channels. The signal is limited by the stochastic boundary for birth energy alphas (~3.52 MeV).

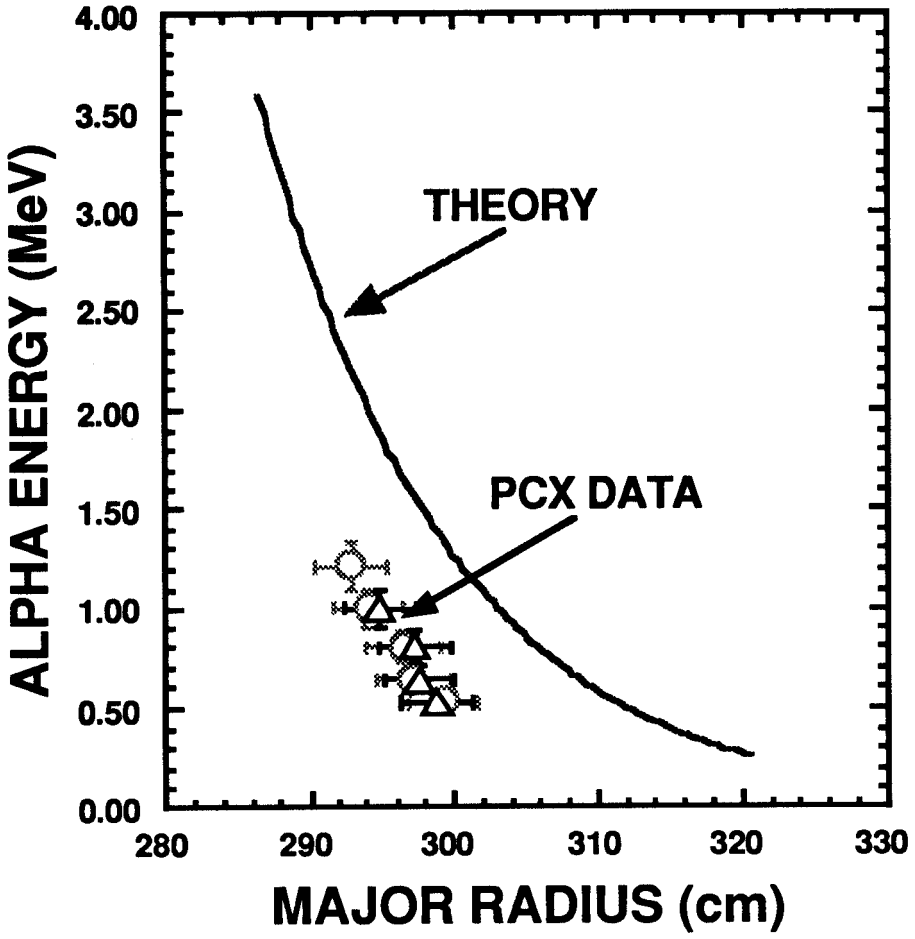

Fig. 9 Measured stochastic ripple boundary as a function alpha energy after sawtooth activity. Sawteeth redistribute low energy alphas beyond the 3.5 MeV birth alpha boundary. Finite orbit effects may account for the disagreement between data and theory.